sciendo

DOI: 10.2478/eces-2025-0012 ECOL CHEM ENG S. 2025;32(2):237-256

Foued CHABANE[1,2*], Ali ARIF[3,4] and Abderrazak GUETTAF[3,4]

AN INNOVATIVE METHOD FOR ESTIMATING AIR TEMPERATURE IN BISKRA USING WEATHER AND AIR POLLUTION

Abstract: This study presents an innovative method for predicting ambient temperature fluctuations using a robust mathematical model that incorporates both environmental pollutants and other meteorological factors across different months. The primary objective was to establish a correlation model that integrates variables such as carbon monoxide, CO, nitrogen dioxide, NO_2, carbon dioxide, CO_2, ozone, O_3, along with model-specific parameters like baseline temperature, Y_0, phase shift, X_c, angular frequency, w, and amplitude, A). Data was collected monthly, from January to June, to analyse the direct impact of these pollutants and parameters on ambient temperature. The correlation constants calculated for each month demonstrate how environmental conditions and pollution levels dynamically influence temperature predictions. Initial findings reveal significant variations in the constants that correlate with changes in pollutant concentrations, suggesting a sensitive interplay between environmental quality and temperature. This study enhances our understanding of temperature dynamics in urban settings and could contribute to more effective environmental monitoring and climate management strategies. The approach underscores the importance of integrating comprehensive environmental data in predictive models to better anticipate temperature changes and potentially mitigate adverse climate impacts.

Keywords: ambient temperature prediction, mathematical modelling, meteorological factors, environmental pollutants, correlation constants

Introduction

The presence of certain pollutants in the air at varying amounts that are hazardous to the health of people, pets, farm animals, plants, soil, and the environment as a whole is referred to as air pollution. External and interior air pollution are the two basic categories of air pollution.

Considering rising atmospheric concentrations of carbon dioxide, methane, and nitrous oxide would raise temperatures globally, therefore increasing continental dryness and possibly reducing area sunlight, these variables could have an impact on the projection of solar radiation. There are numerous air pollutants, such as PM2.5 particles, PM10, sulphur

[1] Department of Mechanical Engineering, Faculty of Technology, University of Biskra, Biskra 07000, Algeria, ORCID: 0000-0002-1363-3371

[2] Mechanical Engineering Laboratory (LGM), Faculty of Technology, University of Biskra, Biskra 07000, Algeria

[3] Department of Electrical Engineering, Faculty of Technology, University of Biskra, Biskra 07000, Algeria, ORCID: AA 0000-0001-6692-8205, AG 0000-0002-2725-0742

[4] Energy Systems Modelling Laboratory (LMSE), Faculty of Technology, University of Biskra, Biskra 07000, Algeria

[*] Corresponding author: fouedmeca@hotmail.fr

dioxide, nitrogen dioxide, carbon monoxide, and ozone O_3, each of which has a distinct effect [1-3].

The mathematical models used examine the current situation, better predict scenarios, and enable preparation and assessment of studies must be accurately developed and evaluated. They are one of the methods for predicting and going to study pollution's impact on temperature, winds, and other factors. Based on this, a study using neural networks and fog systems was carried out in Iran [4]. Researchers to create a model for predicting air pollution [5, 6], used artificial neural networks (*ANN*). A climate investigation and forecasting chemistry model (*WRF-CHEM*) was used in the paper [7] to simulate precipitation and temperature.

To achieve higher accuracy, Ebrahimi and Qaderi [4] concluded that efficient methods should be included in the computational model. Inconsistent qualitative neural inference processes were utilised to adjust for the impacting parameters, like pressure, temperature, and wind speed. A novel computational framework utilising contradictory inferences has been proposed by Khatua et al. [8] to assess the effects of water pollution and global warming on Helsa fish productivity.

It is well known that pollution has an impact on fish output. The model was developed using fuzzy logic and inferred using a tidal method based on fuzzy rules. According to the study [8], although there is a non-linear relationship among the variables, typical time-series prediction methods presume there is one.

Blanes-Vidal et al. [9], used an innovative computational strategy using neuro-fuzzy to examine the effect of nitrogen pollution while contrasting the health repercussions and projections produced from *NFIS* with those gained through true emission distribution. The findings were excellent. By analysing time-series data, the investigation utilising the Neuro-Fuzzy Adjustable aims to improve the accuracy of daily pollutant forecasts [10].

Researchers are looking for an acceptable and precise model of solar radiation since, as we previously stated, the effect of pollution decreases surface solar radiation. Achour et al. [11] evaluated 14 sun radiation models monthly in a study, and the prediction fit for forecasting was selected for the suggested model.

The experiment had conducted in southern Algeria and produced highly encouraging findings. In the same context, the experiment had conducted in Turkey by the researcher Bakirci [12] utilising fifteen solar radiation estimates throughout a protracted time of sunshine. A genuine data set collected at the Applied Research Unit for Renewable Energies (*URAER*) in southern Algeria was used to test the performance of the examined models. Rabehi et al. [13] used this data to forecast daily global sun irradiance (*DGSR*).

During a research report published by Fan et al. [1], the six air pollutants mentioned previously as well as the Air Quality Index (*AQI*) were selected to examine their separate and supportive impacts on the estimated amount of global and diffuse daily solar radiation (*Rs* and *Rd*), The results showed how important it is to choose the appropriate inputs for air pollution. To improve the precision of forecasts, the expected significance of the global time series of solar radiation is forecast using the ARMA and ARIMA models. A method for forecasting the daily and monthly average of global solar irradiance over several months (one, two, and three months) has been suggested by Belmahdi et al. [14].

The newly developed CEEMDAN-CNN-LSTM algorithm for hourly radiation estimated, suggested by Bixuan et al. [15] can be very beneficial for improved smart grid distribution and power generating.

Fen et al. [16] established two distinct approaches for hourly diffusion calculation. Model 1 was a hybrid of four classic models, including Liu and Jordan [17], Orgill and Hollands [18], Erbs et al. [19], and Reindl et al. [20]. utilising sunlight information relating to a model year from Beijing Meteorological as samples for training, the variable was determined by the environment definitions obtained based on the Clarity Index.

Total cloud cover was used in Model 2 to update the classification of weather types, and Principal Component Analysis (*PCA*) was then utilised to further identify the crucial meteorological variables for each weather type as input to the model. Chabane [21] suggested a model for forecasting solar radiation, and it included numerous air contaminants, including CO_2, CO, and CH_4. The Tamanrasset (Algeria) city is the subject of this mathematical model, which considers both diffuse and direct radiation. Our research's goal is to discover a temperature model that considers environmental pollution factors and analyse how such factors affect the ambient temperature in the Biskra. The pollution factors CO_2, O_3, CO, and NO_2 have been introduced as significant parameters to our model.

Complementing this, Bensahal and Yousfi [22] introduced a novel model integrating meteorological parameters and solar radiation to accurately estimate daily air temperatures, enhancing predictive capabilities crucial for climate modelling and environmental management.

Further contributions to the field include Chabane et al. [23] methodology for estimating the distribution of solar radiation using Linke Turbidity Factor and tilt angles, which aids in optimising the installation angles of solar panels to maximise efficiency.

Additionally, Chabane et al. [24] developed a sophisticated theoretical and semi-empirical model of ambient temperature, which significantly aids in understanding and predicting temperature variations influenced by environmental factors. These collective works provide a substantial foundation for advancing renewable energy practices and environmental forecasting.

Recent research highlights the multifaceted impact of air pollution on environmental monitoring, policy, and economic efficiency. Su et al. [25] developed high-resolution air pollution models for California, offering over 30 years of detailed data to analyse long-term trends and inform better air quality management. Liu et al. [26] explored the role of air quality monitoring programs in enhancing transparency and pollution control, showing that public access to pollution data improves regulatory compliance and mitigation efforts. Meanwhile, Li et al. [27] examined how air pollution affects capital allocation efficiency, revealing that poor air quality distorts investment decisions, raises operational costs, and hampers economic productivity. Together, these studies underscore the critical need for robust pollution monitoring, transparent environmental policies, and strategic economic planning to mitigate the far-reaching effects of air pollution.

Recent studies highlight the diverse impacts of air pollution on technology, health, and environmental management. Dudas et al. [28] explored how air pollution reduces the efficiency of photovoltaic systems, using a random forest model to assess the effects of airborne pollutants on solar energy production. Seesaard et al. [29] reviewed advancements in air pollution sensors, emphasising improvements in accuracy and real-time monitoring for better environmental management. Chen et al. [30] analysed the severe health risks associated with air pollution, linking exposure to respiratory and cardiovascular diseases. Meanwhile, Yadav et al. [31] examined the use of artificial neural networks in predicting air pollution levels, demonstrating how *AI*-driven models enhance forecasting and pollution control. Together, these studies underscore the urgent need for improved pollution monitoring, regulatory measures, and technological advancements to mitigate air pollution's wide-ranging effects.

Materials and methods

Study area

Biskra is situated in the southeastern part of Algeria, lying 112 meters above sea level, which positions it among the lowest cities in the country. This region extends over 21,671.20 km^2. According to data collected in 2010, Biskra had a population of approximately 775,797 people, equating to a density of 36 inhabitants per square kilometre on its cultivable land. The climate of Biskra is characterised by its desert environment, featuring mild winters and hot, dry summers. Annually, the temperature averages around 294.05 K, with rainfall ranging from 120 mm to 150 mm, reflecting the arid nature of the region.

Methodology

There are a lot of computational models in the scientific literature. Ours is nonlinear and shaped like a sine curve, with numerous pollution-related components influencing the temperature in Algeria's Biskra region. Considering the temperature variation demonstrated an amazingly flawless convergence with respect to the form proposed from the constant inserted and shared according to this predefined model, we benefited from the relevant constants for application in the final model of mathematics. We utilised contaminating agents that change according to the season and every month of the year.

The creation of a mathematical model that predicts ambient temperature based on pollution parameters is driven by the recognised impact that atmospheric pollutants have on thermal dynamics. This relationship is crucial for understanding how emissions influence climate patterns. Pollutants like carbon dioxide, nitrogen dioxide, and ozone O_3 possess properties that significantly affect atmospheric heat retention and reflection, thereby altering temperatures.

To develop this model, researchers compile extensive datasets on historical temperature readings and pollutant levels, primarily sourced from environmental monitoring stations. They then apply statistical techniques, such as regression analysis, to explore and establish the correlations between temperatures and various pollutants. This process helps quantify how each pollutant contributes to temperature changes, factoring in other environmental variables like solar radiation and wind speed.

In constructing the model, ambient temperature is treated as the dependent variable, with pollutant concentrations as independent variables. The model may include terms for the interaction between pollutants to reflect their combined effects, and non-linear terms might be incorporated to address any non-linear dependencies observed in the preliminary data analysis. More sophisticated models might also leverage machine learning algorithms, which are adept at managing complex variable interactions and enhancing predictive accuracy.

These models are indispensable for forecasting how changes in pollutant levels could affect future temperature patterns, making them essential tools for environmental policy-making and climate research. They not only help predict potential climate changes but also inform strategies for emission reduction and environmental protection.

Mathematical modelling of temperature curves

This flowchart - Figures 1 and 2 - illustrates the steps involved in creating a mathematical model that forecasts ambient temperature using meteorological, astronomical, and atmospheric factors.

In the first step, we enter all the experimental data, including astronomical information about the sun's angle (*h*), the hourly angle (ω), the longitude and altitude of the site control point, the earth's declination, and atmospheric information about pollutants that are relevant to the study site. The final parameter estimates meteorological information, such as the ambient temperature.

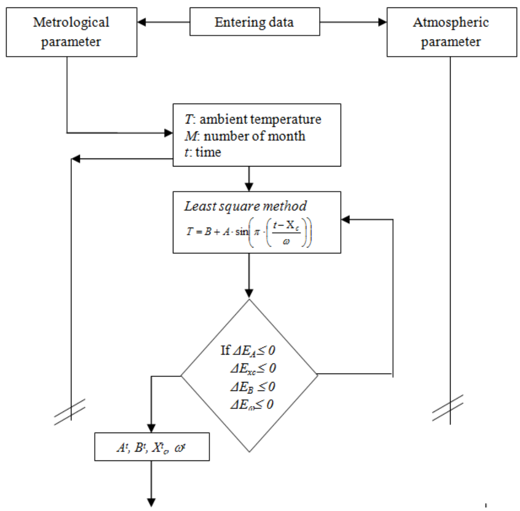

Fig. 1. Organisational program process - part 1

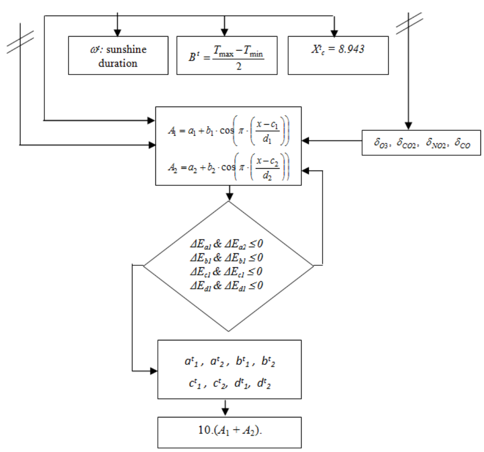

Fig. 2. Organisational program processes - part 2

The program chooses to update the ambient temperature with the number of months, and after that we give the form of a mathematical model when predicting our study in sinusoidal form, using the method of least squares to obtain the constants of the correlation such as A, B, X_c and ω then, we have to check the program errors, such as the constants to get a low error.

The program's second step uses astronomical and meteorological factors to forecast the constants in A that have the form $10 \cdot (A_1 + A_2)$. Then, using the new variable and its connections to other new atmospheric variables such as M_{CO2}, M_{CO}, M_{O3}, M_{NO2}, and the number of months, we are able to derive two mathematical models with the same sinusoidal shape. To obtain a low error, we examined the program's errors, namely those involving the constants a_1, b_1, c_1, and d_1. X_c is a constant value of 8.943 and constant B estimates the deviation of the maximum and minimum ambient temperature divided by two.

Finally, the program produces accurate findings and considers atmospheric, astronomical, and meteorological factors:

M_{CO} - monthly CO content in the air, broken down each month [ppbv],
M_{CO2} - carbon dioxide (CO_2) concentrations in the troposphere [ppmv],
M_{NO2} - tropospheric nitrogen oxides column concentration every month [$10^{15} \cdot$ mol/cm²],
M_{O3} - monthly total column ozone, according to the months [ppbv].

Table 1

Correlation constants for ambient temperature prediction: January to June

Month	**1**	**2**	**3**	**4**	**5**	**6**
y_0	285.22	283.68	286.43	294.03	293.42	307.67
x_c	8.83	9.16	8.64	9.29	8.56	8.77
ω	11.15	8.74	11.28	10.24	12.26	11.35
A	5.32	4.07	7.41	6.72	7.40	8.51
χ^2	1.21	0.86	2.66	0.98	1.11	1.23
R^2	0.925	0.917	0.926	0.960	0.962	0.978
M_{CO}	99.35	102.06	102.54	103.05	95.52	81.21
M_{NO2}	1.30	1.23	1.58	1.16	1.30	0.92
M_{CO2}	400.72	408.13	402.21	403.11	403.78	405.91
M_{O3}	367.71	383.73	422.39	398.68	408.14	387.34

Table 2

Correlation constants for ambient temperature prediction: July to December

Month	**7**	**8**	**9**	**10**	**11**	**12**
y_0	301.83	302.86	304.29	295.74	290.12	284.16
x_c	9.32	9.81	8.67	8.94	8.42	8.90
ω	10.19	11.02	10.55	11.30	9.11	9.26
A	6.20	5.77	5.62	6.57	4.63	3.37
χ^2	0.34	0.93	0.72	1.81	0.67	0.35
R^2	0.984	0.948	0.959	0.926	0.944	0.940
M_{CO}	73.56	73.99	74.80	74.78	83.15	89.01
M_{NO2}	1.165	1.055	1.249	0.952	1.089	1.122
M_{CO2}	399.76	403.02	400.68	399.27	401.02	403.10
M_{O3}	374.41	374.06	362.13	338.35	355.82	367.29

Tables 1 and 2 systematically present comprehensive monthly data on environmental parameters crucial for a model analysing the dynamics of atmospheric conditions. In Table 1, ambient baseline temperatures (y_0) for the first half of the year vary from a low of

283.68 K in February to a high of 307.67 K in June, illustrating significant seasonal warming. The phase shift values (X_c), important for modelling cyclical changes, range from 8.421 in November to 9.81 in August, indicating shifts in peak temperatures throughout the day. Angular frequency (ω), which affects the rate of temperature change, increases from 8.74 in February to 12.26 in May. The amplitude (A), showing temperature variability, peaks at 8.51 in June. The concentrations of pollutants such as carbon monoxide decrease from 102.06 ppm in February to 81.212 ppm in June, while ozone peaks at 422.39 ppb in March, demonstrating the influence of atmospheric chemistry on temperature. Table 2 covers the latter half of the year, where y_0 decreases from 301.83 K in July to 284.16 K in December, reflecting the cooling trend. The amplitude values remain significant, peaking at 6.658 in October, indicating sustained variability in temperatures. These tables offer a detailed view into how environmental and atmospheric parameters are correlated within a predictive model, crucial for understanding temperature dynamics and pollutant impacts over different seasons.

The set of equations you've provided outlines a mathematical model for predicting temperature based on various atmospheric pollutants and other factors. Here's an explanation of each equation:

The equation (1), defines A as ten times the sum of A_1 and A_2, with R^2 indicating the coefficient of determination, which suggests that approximately 79.4 % of the variance in the dependent variable is predictable from the independent variables.

$$A = 10 \cdot (A_1 + A_2) \qquad R^2 = 0.794 \tag{1}$$

Equation (2) represents the first component of A, A_1, modelled as a cosine function influenced by a variable χ, suggesting a periodic component that adjusts based on the phase and amplitude specified.

$$A_1 = \left[-14.78 - 15.56 \cdot \cos\left(\pi \cdot \left(\frac{\chi - 94.02}{-87.74} \right) \right) \right] \tag{2}$$

The second component of A, A_2, is a sine function showing variation over a similar periodic term as A_1, adjusted for different phase and period parameters, which might reflect another cyclic environmental factor affecting the temperature.

$$A_2 = \left[0.124 \cdot \sin\left(2\pi \cdot \left(\frac{\chi - 0.983}{0.95} \right) \right) \right] \tag{3}$$

The equation (4), defines χ as the sum of scaled and normalised differences of several pollutants (M_{O3}, M_{CO2}, M_{NO2}, and M_{CO}) and a number of month M, potentially representing a baseline or mean level of an additional unspecified factor.

$$\chi = \delta_{O3} + \delta_{CO2} + \delta_{NO2} + \delta_{CO} + M \tag{4}$$

Equations (5)-(8) define the δ terms, representing normalised differences for pollutants:

$$\delta_{O3} = \left[\frac{M_{O3} - MIN(M_{O3})}{MAX(M_{O3})} \right] \tag{5}$$

$$\delta_{\mathrm{CO2}} = \left[\frac{M_{\mathrm{CO2}} - MIN(M_{\mathrm{CO2}})}{MAX(M_{\mathrm{CO2}})} \right] \tag{6}$$

$$\delta_{\mathrm{NO2}} = \left[\frac{M_{\mathrm{NO2}} - MIN(M_{\mathrm{NO2}})}{MAX(M_{\mathrm{NO2}})} \right] \tag{7}$$

$$\delta_{\mathrm{CO}} = \left[\frac{M_{\mathrm{CO}} - MIN(M_{\mathrm{CO}})}{MAX(M_{\mathrm{CO}})} \right] \tag{8}$$

A predictive model for temperature T based on the maximum and minimum temperatures scaled around their midpoint, plus a sinusoidal term modified by the combined effects of A_1 and A_2, suggesting the impact of time t and a scaling factor κ on temperature fluctuations.

$$T = \frac{T_{\max} - T_{\min}}{2} + 10 \cdot (A_1 + A_2) \cdot \sin\left(\pi \cdot \left(\frac{t - 8.943}{\kappa} \right) \right) \tag{9}$$

The final link between ambient temperature and atmospheric and astronomical factors is then discovered. See eq. (9), provided the temperature value estimates the meteorological parameter.

$$T_{am} = y_0 + A \cdot \sin\left(\pi \cdot \left(\frac{t - X_c}{\omega} \right) \right) \tag{10}$$

We can infer that the basic theoretical formula, or the initial case, is expressed by formula (10), based on the results in the preceding Tables 1 and 2. The variation, which is the difference divided by two, between the highest and lowest ambient temperatures is stated to be estimated by the constant y_0 of the established model.

$$y_0 = \frac{T_{\max} - T_{\min}}{2} \tag{11}$$

However, we also try to create various models for the relationship constant A (refer to equations (2) and (3)). The novel framework created from A has proven to be the best course of action because the values of A in the table are not consistent during the year.

The key idea is that novel atmospheric conditions related to the existing model are highlighted by equations (4) and (8). The length of the sun relative to the constant might be designated as the variable K.

The equation (12), based on the month of the year, is represented by M. Since M ranges from 1 (January) to 12 (December), the value of ω decreases as the month progresses. In earlier months, when M is smaller, the second term $5.09/M$, contributes significantly, resulting in higher values of ω. As M increases, this term becomes smaller, and ω approaches the constant value of 9.62. This relationship reflects how ω gradually stabilises throughout the year.

$$\omega = 9.62 + \frac{5.09}{M} \tag{12}$$

The data on angular frequency (ω) over the months shows a calculated median value of approximately 10.54, in this part of the research takes the constant value in all months, we can eliminate eq. (12).

Table 3

Monthly performance metrics of temperature forecasting model

Months	χ^2	*RMSE*	*SSE*	R^2
1	1.212	1.278	1.564	0.925
2	0.857	1.999	3.831	0.907
3	2.663	1.725	2.852	0.916
4	0.9784	2.104	4.243	0.961
5	1.107	1.819	3.174	0.962
6	1.229	2.992	8.580	0.969
7	0.340	2.965	8.423	0.984
8	0.926	1.621	2.517	0.949
9	0.719	1.559	2.332	0.959
10	1.812	1.339	1.721	0.926
11	0.673	2.263	4.907	0.944
12	0.354	2.477	5.881	0.944

The model's effectiveness in predicting ambient temperatures is assessed through several statistical metrics as outlined in the provided data. Notably, the model achieves its best performance in July and September, where the reduced χ^2 values are closest to the ideal of 1, recorded at 0.3401 and 0.7196 respectively (see Table 3). These values indicate a high degree of fit between the predicted and observed data, suggesting the model's parameters are well-tuned for these months.

In terms of precision, as measured by the Root Mean Square Error (*RMSE*), the model is most accurate in September, with an *RMSE* of 1.56, see Table 3 pointing to minimal deviation between the forecasted and actual temperatures. This suggests that the model's predictive algorithms are particularly effective during this month, possibly due to more stable or predictable weather patterns.

The Sum of Squares Error (*SSE*), which quantifies the total deviation of the predicted temperatures from the actual values, is also lowest in September at 2.332 (Table 3). This further underscores the model's accuracy during this period.

Moreover, the adjusted R^2, which adjusts the R^2 value to account for the number of predictors in the model, is exceptionally high in July at 0.9864. This statistic highlights the model's ability to explain a significant proportion of the variance in ambient temperatures during this month, reflecting its effectiveness under varying conditions.

Collectively, these metrics illustrate a model that performs exceptionally well in predicting ambient temperatures, particularly during the middle to late summer months. This performance indicates a robust alignment of model parameters with the seasonal dynamics affecting temperature variations, making it an excellent tool for practical applications in climate-sensitive planning and operations.

Results and discussion

Figure 3 displays a detailed visualisation of ambient temperature measurements from January to June, charting daily fluctuations across various months. The temperatures, depicted in a range from 277.5 K to 316 K, exhibit distinct patterns as the year progresses into warmer months. January starts with cooler daily temperatures, averaging around 280 K, gradually increasing to about 291 K by noon. As the season transitions to February, a slight uptick in temperature is noticeable, with afternoon peaks nearing 288 K. March sees a more pronounced rise, with morning temperatures often starting same than

February's peaks and reaching up to 294 K. By April, the trend continues, with temperatures regularly surpassing 300 K, particularly in the afternoons. May shows significant warmth, with noon temperatures frequently touching 301 K, reflecting the approach of summer. June, the warmest month in this period, often sees temperatures peaking around 316 K around midday, illustrating the typical climatic shift towards higher temperatures as summer sets in fully. This graphically represented data captures the essence of seasonal temperature progression, providing valuable insights into monthly climatic changes and their impact on daily temperature behaviour.

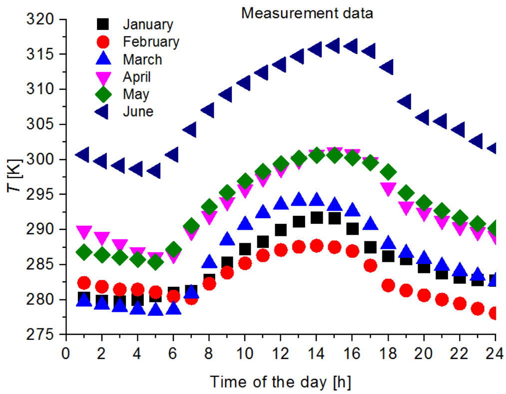

Fig. 3. The beginning six-month period of ambient temperatures as a function of the daily conditions, as measured experimentally

Figure 4 presents forecasted ambient temperatures for the first six months of the year, demonstrating the model's ability to predict daily temperature patterns from January to June. The data illustrates a progressive increase in temperature as the months advance, closely mirroring the seasonal transition from winter to summer. January's forecast shows temperatures starting from just above 280 K in the early morning and peaking at around 290 K by midday. February displays a slight warming trend with peaks reaching approximately 288 K. In March, the model predicts a sharper rise in morning temperatures with noon peaks climbing to about 294 K. April and May see a more pronounced increase, with temperatures in May soaring up to 315 K around midday, indicating the onset of warmer weather. June, consistently showing the highest temperatures, predicts midday peaks nearing 299 K, showcasing the typical peak of summer warmth. This forecast data not only validates the model's accuracy in capturing daily and seasonal fluctuations but also serves as a tool for preparing for climatic changes that impact various environmental and economic sectors.

Figure 5 captures the variation in ambient temperatures over the latter half of the year, from July to December, as recorded through daily measurements. This graphical representation indicates the seasonal transition from the warm summer months back to cooler winter conditions. August and September display the highest temperatures of the year, with daily peaks often reaching around 310 K, especially evident in the red circles (August) and blue triangles (September), and black squares (July), highlighting the intense summer heat. As the season progresses into October and November, represented by pink inverted triangles and green diamonds respectively, there is a noticeable decrease in peak temperatures, dipping to about 302 K and further cooling to around 295 K in November. Moving into the cooler months of November and December, marked by green diamonds and dark blue triangles facing left, the data shows a more pronounced drop, with temperatures rarely climbing above 290 K and reaching lows near 280 K in the early morning hours. This dataset provides valuable insights into the diurnal and seasonal temperature dynamics, critical for understanding climate patterns and planning related to energy consumption, agriculture, and environmental management.

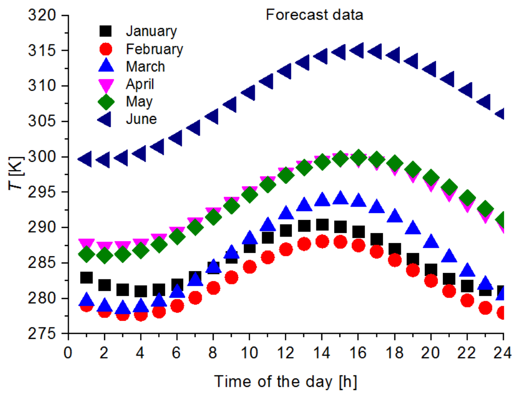

Fig. 4. The relationship between ambient temperatures and daily weather conditions during the initially six months (forecast data)

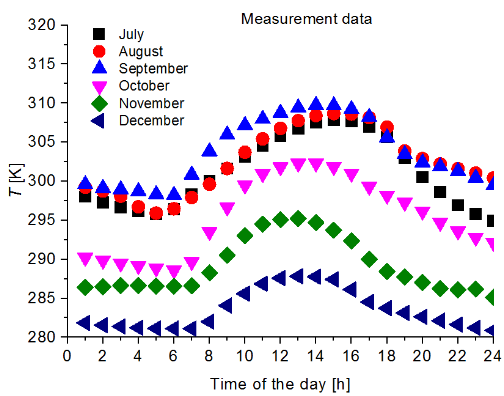

Fig. 5. The second set includes six months' worth of data on ambient temperatures as a consequence of everyday conditions (experimental measurement)

Figure 6 illustrates the forecasted ambient temperatures for the latter half of the year, spanning from July to December, and captures the cyclical nature of daily temperatures as influenced by changing weather conditions. In July, the model predicts high temperatures, with daily peaks reaching up to 310 K, shown by the blue triangles, indicating the height of summer. As the months progress, there is a noticeable cooling trend. August temperatures (red circles) remain high but start to show a decline, particularly towards the end of the day. October and November represented by pink inverted triangles and green diamonds respectively, exhibit a further reduction in temperature, aligning with the onset of autumn. October maintains a warmer midday temperature around 300 K but cools significantly by evening. November sees a more pronounced drop, with temperatures seldom rising above 295 K. The forecast for November and December (blue and black diamonds, respectively) shows a continued decrease in temperatures, aligning with the approach of winter. November days start cooler at around 290 K and decrease further in December, where temperatures hover around 285 K, even dipping below this mark during early morning and late evening hours.

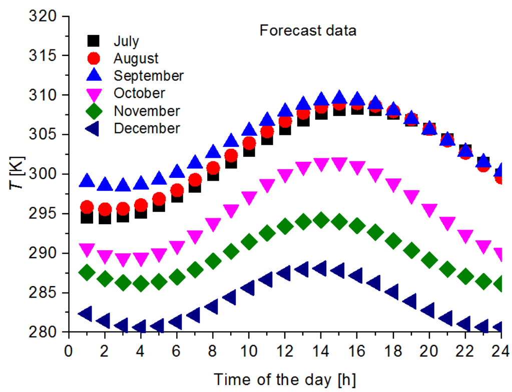

Fig. 6. The following two six months' worth of forecasting data show the relationship between ambient temperatures and everyday weather

The development of ambient temperature has been impacted by fluctuations in atmospheric factors and the environment. We also take into consideration the astronomical influence of daylight length of time, particularly is related to the Earth's and the sun's movements (see Figure 13). Polluting criteria were added, and the result was the creation of extremely sensitive, excellent, and actual factors, which translated into a similarity between the computerised and experimental.

The latter causes an observable increase in September's ambient temperature over previous months, which can be attributed to the effect of rising pollutant values, which are calculated using CO (75 ppbv), CO_2 (400.5 ppmv) and NO_2 ($1.25 \cdot 10^{15}$ molecules/cm^2).

Figure 7 illustrates the variation in monthly carbon monoxide (CO) concentrations throughout the year, expressed in parts per billion by volume (ppbv). This graph depicts a sinusoidal pattern, peaking during the early months and then gradually declining. The highest CO levels are observed in April, reaching approximately 103 ppbv, suggesting increased emissions or reduced atmospheric dispersion during this time. As the months progress into summer and early autumn, there is a noticeable decrease in CO levels, with concentrations dropping to around 73.56 ppbv by July. This trend reverses slightly in the later months, where CO concentrations begin to rise again, ending the year at around 89 ppbv in December. The sinusoidal pattern may reflect seasonal variations in factors such as fuel combustion rates, atmospheric conditions, or regulatory measures affecting CO emissions.

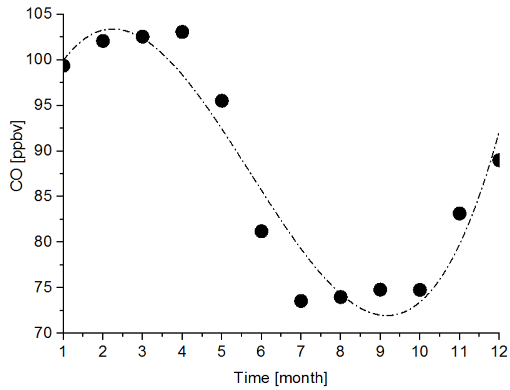

Fig. 7. Monthly variation of atmospheric column CO concentration

Figure 8 presents a detailed analysis of the monthly variations in nitrogen dioxide (NO_2) concentrations in the troposphere throughout the year, quantified in molecules per cm^2. The graph shows a dynamic pattern in NO_2 levels, characterised by periodic fluctuations that suggest strong seasonal influences. Beginning the year, NO_2 concentrations are relatively high in February, peaking at approximately $1.6 \cdot 10^{15}$ molecules/cm². The levels then exhibit a significant decline, reaching a low of around $0.9 \cdot 10^{15}$ molecules/cm² by June, which might reflect reduced heating emissions and the onset of warmer weather which can change atmospheric dispersion patterns.

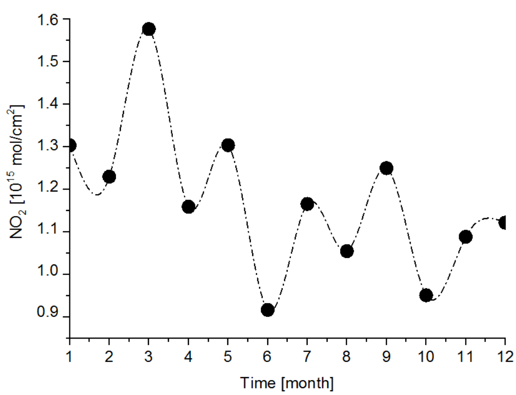

Fig. 8. Troposphere nitrogen oxides column concentration every month, by month

The concentrations rebound in May, climbing back to around $1.3 \cdot 10^{15}$ molecules/cm^2, possibly due to increased activity as temperatures rise, before gradually tapering off into the summer months. Notably, the lowest point occurs in June and October, suggesting a minimal level of emissions or effective atmospheric cleansing processes during this period. As the year progresses into autumn and winter, NO_2 levels begin to rise again, ending the year on a higher note in December, close to the initial values seen in January. This annual cycle is likely driven by a combination of meteorological conditions, such as temperature and wind patterns, along with seasonal variations in emissions from heating, traffic, and industrial activities.

The reason for this transition may be found in Figure 8, where the determined point of nitrogen oxides in September approaches an amount of $1.25 \cdot 10^{15}$ molecules/cm^2), approximately is comparable to the highest level of July and August. Equation (7), indicating a novel parameter connecting the highest and lowest nitrogen oxide amounts, is the outcome of all of this. The newly introduced factor nitrogen oxides are added to the three formulas - (2), (3), and (4).

Figure 9 depicts the monthly variations in carbon dioxide (CO_2) concentrations in the troposphere, measured in parts per million by volume (ppmv). This detailed graph indicates a fluctuating pattern of CO_2 levels throughout the year, reflecting both seasonal effects and anthropogenic influences on atmospheric composition. The year starts with a higher concentration around 408 ppmv in February, which slightly decreases in March. A noticeable uptick occurs from April and May, peaking in June at approximately 406 ppmv, potentially linked to increased fossil fuel consumption as temperatures are still low.

Following this spring peak, CO_2 levels show a sharp decrease into the summer months, dipping to their lowest in July at about 399 ppmv, which may be due to enhanced vegetation growth absorbing more CO_2 during the peak growing season. However, as autumn approaches and photosynthetic activity decreases, CO_2 levels start to rise again, evidenced by the gradual increase from August through November, culminating in a higher concentration towards the end of the year. The cyclic rise in late autumn and winter could also be influenced by increased heating emissions and reduced atmospheric mixing. This pattern aligns with global observations linking seasonal biological cycles and human activities to variations in atmospheric CO_2 levels.

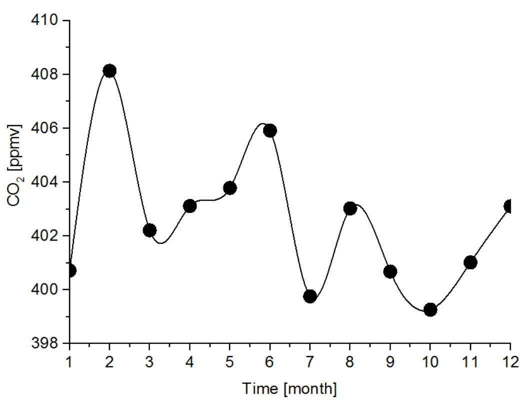

Fig. 9. The months' worth of carbon dioxide in the troposphere each month

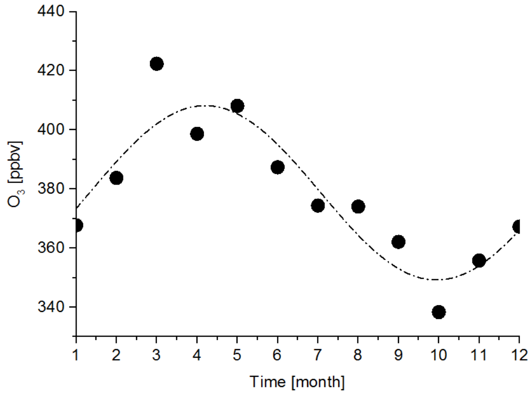

Fig. 10. Monthly total column ozone, according to the months

Figure 10 provides a detailed depiction of the monthly variations in total column ozone measured in parts per billion by volume (ppbv) throughout the year. The graph shows a sinusoidal trend in ozone concentrations, which peaks during the early months and gradually diminishes as the year progresses, before rising again towards the end of the year.

In January, ozone levels start at their low, around 367.7 ppbv, suggesting strong atmospheric presence possibly due to lower temperatures reducing the ozone decomposition rate and lesser sunlight to catalyse the breakdown of ozone. As the months move into spring and early spring, there is a marked increase in ozone levels, reaching the highest point in March at approximately 422.4 ppbv. This decline could be attributed to increased sunlight during these months, which enhances ozone decomposition rates.

As summer transitions into autumn, the ozone levels start to recover, showing a gradual increase through September, and November. This increase might be influenced by decreasing temperatures and changing sunlight conditions, which reduce the rate of ozone breakdown. By December, the levels approach the values observed at the beginning of the year, completing an annual cycle. This pattern highlights the dynamic nature of ozone as a seasonal and environmentally reactive atmospheric component, influenced by temperature, sunlight, and human-induced changes in the atmosphere.

March through October has the most variations in ozone, with a peak of 422 ppbv in March and a low of 338.35 ppbv in October.

The newly introduced variable indicates that this variation is included and is connected by the zone's highest and lowest values. Refer to formula (5), which is incorporated into formulas (2), (3), and (4).

Figure 11 illustrates the effects of two different modelling approaches on the calculated amplitude parameter A in a monthly ambient temperature model, considering the impacts of both atmospheric ozone levels and additional pollution factors. The black bars represent the model outputs without considering pollution elements, whereas the red bars include the effects of pollution, specifically scaled by a factor of $10 \cdot (A_1 + A_2)$, where A_1 and A_2 are coefficients from pollution-dependent terms in the model.

Throughout the year, the values of A vary significantly, showing higher values when pollution factors are considered, especially noticeable from March to September. The peak occurs in July, indicating the highest influence of pollutants on temperature amplitude, reaching nearly 8 on this scale. In contrast, the model without pollutants shows a more subdued variation, peaking around 5.5, also in July.

This distinct difference underscores the significant impact of including pollution parameters in temperature forecasting models. The presence of pollutants tends to enhance the amplitude of temperature variations, suggesting that pollution not only affects air quality but also modifies the thermal dynamics of the atmosphere. This model provides a clear visual representation of how environmental pollutants can dramatically alter temperature behaviours, which is crucial for developing more accurate climate models and understanding the broader impacts of environmental pollution.

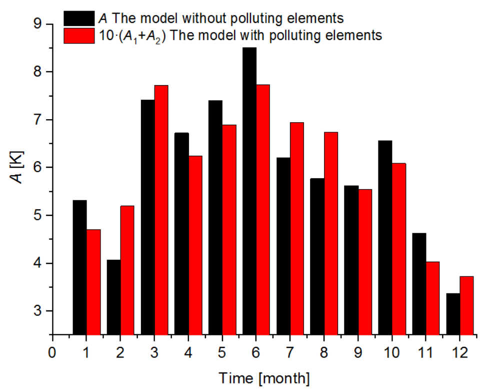

Fig. 11. Two different modelling approaches, according to the months

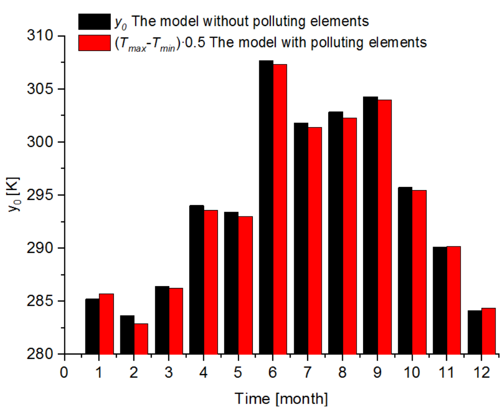

Fig. 12. A constant of the y_0, and $(T_{max} - T_{min})/2$, according to the months

Figure 12 shows the variations in the constant y_0 across the months, with and without considering pollution elements, expressed in terms of the average temperature deviation see eq. (11). In this bar graph, the black bars represent the model without pollution effects, and the red bars represent the model incorporating pollution effects, where the deviation is adjusted by multiplying by 0.5.

The data reveals a clear seasonal pattern with both models showing higher values in the warmer months and lower values during the cooler months. The pollution model consistently shows higher deviations, indicating that pollution factors lead to greater temperature variability within a day. For example, during the peak month of July, the deviation reaches above 301 in the pollution model, suggesting that pollutants significantly amplify daily temperature swings. Conversely, during January, the deviation is at its lowest, hovering around 283, indicating minimal temperature variation.

This enhanced amplitude in the pollution model illustrates how atmospheric pollutants can exacerbate temperature extremes, leading to larger diurnal temperature variations. Such information is vital for understanding how pollution not only deteriorates air quality but also impacts thermal comfort and energy consumption patterns across different times of the year.

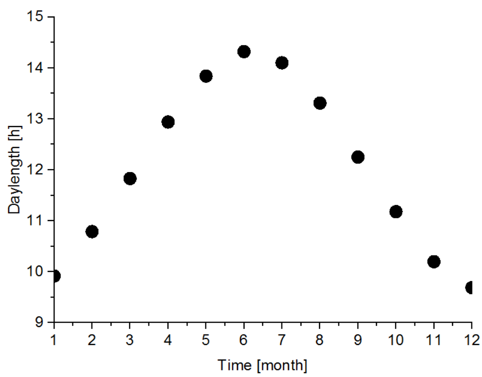

Fig. 13. Daylength, according to the months

Figure 13 provides a detailed view of how daylength varies throughout the year, mapped month by month. Starting in January, the daylength is approximately 10 hours and gradually increases as the month's progress. By March, the daylength reaches about 11.85 hours, aligning with the spring equinox when day and night are approximately equal. This increasing trend continues, with daylength peaking in June, where it reaches roughly 14.3 hours, coinciding with the summer solstice - this is the longest day of the year in the Northern Hemisphere due to the Earth tilting most directly towards the sun.

After June, the daylength begins to decline, reflecting the approach towards autumn. By September, the daylength reduces back to around 12 hours, marking the autumnal equinox, and continues to decrease into the winter months. December shows the shortest daylength, dropping to about 9.67 hours, which corresponds to the winter solstice. During this time, the Northern Hemisphere is tilted away from the sun, resulting in the shortest days of the year.

Understanding these changes is crucial for various practical applications. In agriculture, the knowledge of daylight hours helps in scheduling the planting and harvesting of crops, as growth cycles are closely linked to light exposure. Energy sectors also benefit from this data, as longer daylight reduces the dependency on artificial lighting, thereby influencing energy consumption strategies. Moreover, these patterns are significant for ecological and environmental studies, where animal behaviours and other ecological processes are deeply intertwined with seasonal light variations. This detailed monthly breakdown of daylength provides essential insights for industries and researchers who rely on accurate daylight information to guide their activities and studies.

Conclusion

A conclusion that tries to investigate how to categories ambient temperature according to many criteria, such as the conditions astronomical, atmospheric, and meteorological, which greatly aids us in comprehending all the environmental influences on the temperature of the atmosphere. The ambient temperature changes depending on where you are in industrial areas, rural areas, and heavily inhabited areas, whether it rises or falls.

Keeping in mind that the sun's influence on the environment's temperature is important, the degree to which the atmosphere is clear, overcast, or partly cloudy depends on the nature of the atmosphere.

Given the effects of global warming, particularly global warming, these reasons are air pollutants brought on by the use of fuels and chemicals in the most industrialised regions. We made an effort to correlate temperature with all the effects of pollutants, such as M_{CO2} concentration in the air and tropospheric CO_2 levels, total column ozone, tropospheric M_{NO2} column density, and total column ozone. The greenhouse effect causes the atmosphere to become opaque to solar energy. Pollution is the source of the latter. It plays a crucial part in raising the temperature. In this study, we demonstrated how environmental pollution-related characteristics affect the local temperature in the Biskra region of Algeria.

The mathematical model found is highly useful in the computation and prediction since the correlation under pollution offered values for each month of the year that was very near to the experimental.

Acknowledgements

The My NASA Data initiative, developed by the United States' National Aeronautics and Space Administration (NASA), enables researchers around the world to analyse data more effectively. This online platform allows scholars to easily locate areas of interest and access relevant scientific information associated with specific coordinates.

References

[1] Fan J, Wu L, Zhang F, Cai H, Wang X, Lu X, et al. Evaluating the effect of air pollution on global and diffuse solar radiation prediction using support vector machine modeling based on sunshine duration and air temperature. Renew Sust Energy Rev. 2018;94:732-47. DOI: 10.1016/j.rser.2018.06.029.

[2] Kalisa E, Fadlallah S, Amani M, Nahayo L, Habiyaremye G. Temperature and air pollution relationship during heatwaves in Birmingham, UK. Sust Cities Soc. 2018;43:111-20. DOI: 10.1016/j.scs.2018.08.033.

[3] Lee W, Choi HM, Kim D, Honda Y, Guo Y-LL, Kim H. Synergic effect between high temperature and air pollution on mortality in Northeast Asia. Environ Res. 2019;178:108735. DOI: 10.1016/j.envres.2019.108735.

[4] Ebrahimi M, Qaderi F. Determination of the most effective control methods of SO_2 pollution in Tehran based on adaptive neuro-fuzzy inference system. Chemosphere. 2021;263:128002. DOI: 10.1016/j.chemosphere.2020.128002.

[5] Cabaneros SM, Calautit JK, Hughes BR. A review of artificial neural network models for ambient air pollution prediction. Environ Modelling Software. 2019;119:285-304. DOI: 10.1016/j.envsoft.2019.06.014.

[6] Samakosh JD, Mirzaie M. Flash-over voltage prediction of silicone rubber insulators under longitudinal and fan-shaped non-uniform pollution condition. Computers Electrical Eng. 2019;78:50-62. DOI: 10.1016/j.compeleceng.2019.07.004.

[7] Amnuaylojaroen T, Macatangay RC, Khodmanee S. Modeling the effect of VOCs from biomass burning emissions on ozone pollution in upper Southeast Asia. Heliyon. 2019;5:e02661. DOI: 10.1016/j.heliyon.2019.e02661.

[8] Khatua A, Jana S, Kar TK. A fuzzy rule-based model to assess the effects of global warming, pollution and harvesting on the production of Hilsa fishes. Ecol Informatics. 2020;57:101070. DOI: 10.1016/j.ecoinf.2020.101070.

[9] Blanes-Vidal V, Cantuaria ML, Nadimi ES. A novel approach for exposure assessment in air pollution epidemiological studies using neuro-fuzzy inference systems: Comparison of exposure estimates and exposure-health associations. Environ Res. 2017;154:196-203. DOI: 10.1016/j.envres.2016.12.028.

[10] Masoomeh Z, Abdoulmohammad GC, Feybi AG, Jirí JK. Air pollution prediction using semi-experimental regression model and Adaptive Neuro-Fuzzy Inference System. J Cleaner Prod. 2020;261:121218. DOI: 10.1016/j.jclepro.2020.121218.

[11] Achour L, Bouharkat M, Assas O, Behar O. Hybrid model for estimating monthly global solar radiation for the Southern of Algeria (Case study: Tamanrasset, Algeria). Energy. 2017;135:526-39. DOI: 10.1016/j.energy.2017.06.155.

[12] Bakirci K. Models for the estimation of diffuse solar radiation for typical cities in Turkey. Energy. 2015;82:827-38. DOI: 10.1016/j.energy.2015.01.093.

[13] Rabehi A, Guermoui M, Lalmi D. Hybrid models for global solar radiation prediction: case of study. Int J Ambient Energy. 2020;41:31-40. DOI: 10.1080/01430750.2018.1443498.

[14] Belmahdi B, Louzazni M, El Bouardi A. One month-ahead forecasting of mean daily global solar radiation using time series models. Optik - Int J Light Electron Optics. 2020;219:165-207. DOI: 10.1016/j.ijleo.2020.165207.

[15] Bixuan G, Xiaoqiao H, Junsheng S, Yonghang T, Jun Z. Hourly forecasting of solar irradiance based on CEEMDAN and multi-strategy CNNLSTM neural networks. Renew Energy. 2020;162:1665-83. DOI: 10.1016/j.renene.2020.09.141.

[16] Fen L, Yilun L, Jianping G, Yue W, Ling M, Yang C, et al. Novel models to estimate hourly diffuse radiation fraction for global radiation based on weather type classification. Renew Energy. 2020;157:1222-32. DOI: 10.1016/j.renene.2020.05.080.

[17] Liu BYH, Jordan RC. The interrelationship and characteristic distribution of direct, diffuse, and total solar radiation. Solar Energy. 1960;4:1-19. DOI: 10.1016/0038-092X(60)90062-1.

[18] Orgill JF, Hollands KGT. Correlation equation for hourly diffuse radiation on horisontal surface. Solar Energy. 1977;19(4):357-9. DOI: 10.1016/0038-092X(77)90006-8.

[19] Erbs DG, Klein SA, Duffie JA. Estimation of the diffuse radiation fraction for hourly, daily and monthly-average global radiation. Solar Energy. 1982;28(4):293-302. DOI: 10.1016/0038-092X(82)90302-4.

[20] Reindl DT, Beckman WA, Duffie JA. Diffuse fraction correlation. Solar Energy. 1990;45(1):1-7. DOI: 10.1016/0038-092X(90)90060-P.

[21] Chabane F. Estimation of direct and diffuse solar radiation on the horisontal plane considering air quality index and turbidity factor in Assekrem, Tamanrasset, Algeria. Air Quality, Atmosphere Health. 2020;13:1505-16. DOI: 10.1007/s11869-020-00904-9.

[22] Bensahal D, Yousfi A. A new model to estimate the daily air temperature using the meteorological parameters and global solar radiation. Iran J Sci Technol Trans Mech Eng. 2023;47:1467-74. DOI: 10.1007/s40997-022-00583-0.

[23] Chabane F, Moummi N, Brima A. A new approach to estimate the distribution of solar radiation using Linke turbidity factor and tilt angle. Iran J Sci Technol Trans Mech Eng. 2021;45:523-34. DOI: 10.1007/s40997-020-00382-5.

[24] Chabane F, Moummi N, Brima A, Moummi A. Prediction of the theoretical and semi-empirical model of ambient temperature. Front Energy. 2016;10:268-76. DOI: 10.1007/s11708-016-0413-y.

[25] Su JG, Shahriary E, Sage E, Jacobsen J, Park K, Mohegh A. Development of over 30-years of high spatiotemporal resolution air pollution models and surfaces for California. Environ Int. 2024;193:109100. DOI: 10.1016/j.envint.2024.109100.

[26] Liu Y, Liu W, Chen X, Fang R, Deng L. The synergies of air quality monitoring program: Information disclosure and pollution control. J Environ Manage. 2025;375:124258. DOI: 10.1016/j.jenvman.2025.124258.

[27] Li Y, Hu W, Jiang Y. How does air pollution affect capital allocation efficiency? Ecol Indicators. 2024;158:111617. DOI: 10.1016/j.ecolind.2024.111617.

[28] Dudáš A, Udristioiu MT, Alkharusi T, Yildishan H, Sampath SK. Examining effects of air pollution on photovoltaic systems via interpretable random forest model. Renew Energy. 2024;232:121066. DOI: 10.1016/j.renene.2024.121066.

[29] Seesaard T, Kamjornkittikoon K, Wongchoosuk C. A comprehensive review on advancements in sensors for air pollution applications. Sci Total Environ. 2024;951:175696. DOI: 10.1016/j.scitotenv.2024.175696.
[30] Chen F, Zhang W, Mfarrej MFB, Saleem MH, Khan KA, Ma J, et al. Breathing in danger: Understanding the multifaceted impact of air pollution on health impacts. Ecotoxicol Environ Safety. 2024;280:116532. DOI: 10.1016/j.ecoenv.2024.116532.
[31] Yadav V, Yadav AK, Singh V, Singh T. Artificial neural network an innovative approach in air pollutant prediction for environmental applications: A review. Results Eng. 2024;22:102305. DOI: 10.1016/j.rineng.2024.102305.